EcoEnergy

WILEY

EcoEnergy Open Access

RESEARCH ARTICLE OPEN ACCESS

Boosting Charge Separation in a $CdIn_2S_4/Mo_2TiC_2$ MXene Schottky Heterojunction for Enhanced Photocatalytic Hydrogen Production

Bingzhu Li[1] | Teng Li[2] | Xiaohua Ma[1] | Minjun Lei[1] | Zhiliang Jin[1] | Noritatsu Tsubaki[2] | Paolo Fornasiero[3]

[1]School of Chemistry and Chemical Engineering, Ningxia Key Laboratory of Solar Chemical Conversion Technology, Key Laboratory for Chemical Engineering and Technology, State Ethnic Affairs Commission, North Minzu University, Yinchuan, China | [2]Department of Applied Chemistry, Graduate School of Engineering, University of Toyama, Toyama, Japan | [3]Department of Chemical and Pharmaceutical Sciences, Center for Energy, Environment and Transport Giacomo Ciamician, INSTM Trieste Research Unit and ICCOM-CNR Trieste Research Unit, University of Trieste, Trieste, Italy

Correspondence: Xiaohua Ma (mxh6464@163.com) | Zhiliang Jin (zl-jin@nun.edu.cn) | Paolo Fornasiero (pfornasiero@units.it)

Received: 5 November 2025 | **Revised:** 16 January 2026 | **Accepted:** 10 February 2026

Keywords: $CdIn_2S_4$ | Mo_2TiC_2 MXene | photocatalytic hydrogen evolution | Schottky heterojunction

ABSTRACT

Mo_2TiC_2 MXene was exfoliated in situ using hydrofluoric acid solution and subsequently integrated with $CdIn_2S_4$ through physical stirring and grinding. The composite material demonstrated exceptional photocatalytic hydrogen evolution (PHE) activity without the loading of any noble metal co-catalysts, achieving a hydrogen production rate as high as 3.35 $mmol \cdot h^{-1}\ g^{-1}$. This represents a 55.83-fold enhancement compared to pristine $CdIn_2S_4$ and surpasses the performance of most reported $CdIn_2S_4$-based photocatalytic materials. Furthermore, the composite material maintained consistent hydrogen evolution performance throughout four consecutive cycling tests, demonstrating excellent cycling durability. Through systematic experimental analysis and theoretical simulations, it was confirmed that a Schottky heterojunction forms between $CdIn_2S_4$ and Mo_2TiC_2 MXene. In this composite system, $CdIn_2S_4$ primarily serves as the light-absorbing component, whereas Mo_2TiC_2 MXene functions as an efficient co-catalyst. The formation of the Schottky junction drives the directional migration of photogenerated electrons from $CdIn_2S_4$ to Mo_2TiC_2 MXene. The resulting interfacial potential barrier significantly suppresses electron backflow, whereas the inherent high electrical conductivity of Mo_2TiC_2 MXene and its abundant exposed active sites further accelerate the hydrogen evolution process. This study demonstrates the significant potential of Mo_2TiC_2 MXene as a novel co-catalyst for photocatalysis oriented toward renewable energy.

1 | Introduction

The contradiction between rising global energy demand and the depletion of fossil fuels and environmental deterioration is becoming increasingly acute [1, 2]. The development of clean and renewable energy sources is imperative for achieving sustainable development [3]. Hydrogen energy is lauded as an ideal and the most promising energy carrier, by virtue of its high energy density, zero-carbon emissions, and sole production of water [4, 5]. Presently, more than 95% of hydrogen originates from fossil fuel reforming, which generates a large amount of CO_2 emissions and does not fall under the category of green hydrogen [6]. Therefore, employing renewable energy to power water splitting for green hydrogen production represents a pivotal strategy to tackle concurrent energy and environmental challenges [7]. Among them, solar-driven photocatalytic water splitting for hydrogen production technology can directly convert abundant solar energy into chemical energy (hydrogen energy), and the reaction process is

Bingzhu Li and Teng Li are equal contributors.

environmentally friendly and green, and is considered a highly promising low-carbon hydrogen production approach [8]. PHE technology mimics natural photosynthesis by utilizing a semiconductor photocatalyst. Upon irradiation with sunlight of energy exceeding its bandgap, electron-hole pairs are generated. These charge carriers then drive redox reactions, with electrons facilitating proton reduction and holes mediating water oxidation [9, 10]. This technology theoretically only uses water and sunlight as raw materials, and the reaction conditions are mild, making it an extremely attractive low-cost hydrogen production solution [11, 12].

However, the widespread implementation of this technology is still hampered by the performance of photocatalysts [13, 14]. Addressing the core challenge requires the concurrent realization of efficient solar light capture, charge separation, and surface hydrogen evolution reaction (HER) kinetics [15]. The ternary chalcogenide $CdIn_2S_4$ has emerged as a promising candidate for PHE owing to its unique physical and chemical properties [16, 17]. Firstly, it has an appropriate band gap of approximately 2.0–2.4 eV, which enables it to effectively absorb visible light and even some near-infrared light, significantly improving the utilization efficiency of solar energy [18]. Secondly, compared with CdS which is prone to photo-corrosion, the crystal structure of $CdIn_2S_4$ is more stable. The In^{3+} ions in it can effectively inhibit the photo-dissolution of Cd^{2+}, demonstrating excellent resistance to photo-corrosion and long-term stability [19]. Although $CdIn_2S_4$ has the aforementioned advantages, its photogenerated carrier separation efficiency still needs to be further improved, and the insufficient surface active sites also limit the full performance of its HER [20].

Introducing co-catalysts to construct Schottky heterojunctions is an effective strategy [21]. The barrier formed at the metal-semiconductor interface can facilitate one-way transport of photogenerated electrons and maximally suppress electron-hole recombination, ultimately significantly enhancing the utilization efficiency of photogenerated charges [22]. In recent years, MXene, a novel two-dimensional material renowned for its high conductivity and strong electron-accepting ability, has found extensive applications in fields including supercapacitors, lithium batteries, electrocatalysis, and photocatalysis [23]. Among them, Mo_2TiC_2 MXene, with its unique layered structure, excellent conductivity, rich surface chemical properties and controllable electronic structure, has laid a solid foundation for the construction of efficient photocatalytic systems [24]. Compared with traditional catalysts, Mo_2TiC_2 MXene possesses a higher specific surface area and more exposed active sites, thus promoting the adsorption and activation of reactant molecules and enabling the construction of intimate heterojunctions with other semiconductors for enhanced carrier separation and transport [25]. On the other hand, using Mo_2TiC_2 MXene with a large specific surface area as a carrier can anchor small-sized semiconductor nanomaterials through interfacial effects, effectively mitigating their aggregation problem and thereby ensuring the stability of active sites and the reaction efficiency during the photocatalytic process [26].

This study successfully fabricated a Schottky heterojunction photocatalyst by integrating HF-etched Mo_2TiC_2 MXene with $CdIn_2S_4$ nanospheres via physical stirring and grinding. Characterization results revealed that the heterostructure effectively modulates the band alignment between the two components, establishing a significant interfacial potential difference that drives directional charge separation. The established Schottky junction facilitates efficient interfacial charge transfer, wherein Mo_2TiC_2 MXene acts as an effective co-catalyst to capture photogenerated electrons from $CdIn_2S_4$ and suppress charge recombination. Consequently, the $CdIn_2S_4$/Mo_2TiC_2 MXene composite exhibits remarkable photocatalytic activity. This work not only proposes a novel strategy for designing high-performance $CdIn_2S_4$-based photocatalysts but also provides fundamental insights into the reaction mechanism of Schottky heterojunctions.

2 | Experimental Section

2.1 | Preparation of $CdIn_2S_4$

In a typical synthesis, 1 mmol $CdCl_2$, 2 mmol $InCl_3$, and 5 mmol thioacetamide were dissolved in 30 mL deionized water under stirring. After complete dissolution, 7 mmol NaOH was introduced, yielding a yellow suspension. This suspension was then transferred to a 50 mL autoclave and maintained at 180°C for 12 h. The resulting product was collected via centrifugation after cooling, washed repeatedly with deionized water and ethanol, and dried at 70°C to obtain the final yellow $CdIn_2S_4$.

2.2 | Preparation of Mo_2TiC_2 MXene

In a 100 mL polytetrafluorethylene-lined container, add 15 mL (40%) HF and 15 mL water. Weigh 2 g of Mo_2TiAlC_2 powder and slowly add it to the reaction vessel in batches. The reaction was stirred at 40°C for 48 h, followed by centrifugation of the resulting slurry to obtain a viscous precipitate. Then, add 30 mL of 10% TMAOH solution to the centrifuge tube, ultrasonicate, and transfer it to a 100 mL beaker. Stir at room temperature for 12 h (sealed with plastic film). After the stirring is completed, centrifuge again and wash. The final product is dried for 2 h in a vacuum environment at 60°C, and then can be obtained as Mo_2TiC_2 MXene.

2.3 | Preparation of $CdIn_2S_4$/Mo_2TiC_2 MXene

The $CdIn_2S_4$/Mo_2TiC_2 MXene composite material was prepared by combining physical stirring and grinding. A mixture of $CdIn_2S_4$ (50 mg) and Mo_2TiC_2 MXene (1 mg) was subjected to ultrasonic treatment in 30 mL of anhydrous ethanol for 10 min to ensure uniform dispersion. Then, they were continuously stirred for 3 h. The resulting mixture was stirred in an 80°C water bath and evaporated to complete dryness, and then transferred to a mortar for thorough grinding. Finally, 20 wt% Mo_2TiC_2 MXene/$CdIn_2S_4$ (named CMT-20) was obtained. By adjusting the mass ratio of Mo_2TiC_2 MXene to $CdIn_2S_4$, different Mo_2TiC_2 MXene contents were prepared, including 5 wt%, 10 wt%, 15 wt%, and 25 wt% Mo_2TiC_2 MXene/$CdIn_2S_4$ samples, named CMT-5, CMT-10, CMT-15, and CMT-25, respectively. The specific preparation process is shown in Figure 1a.

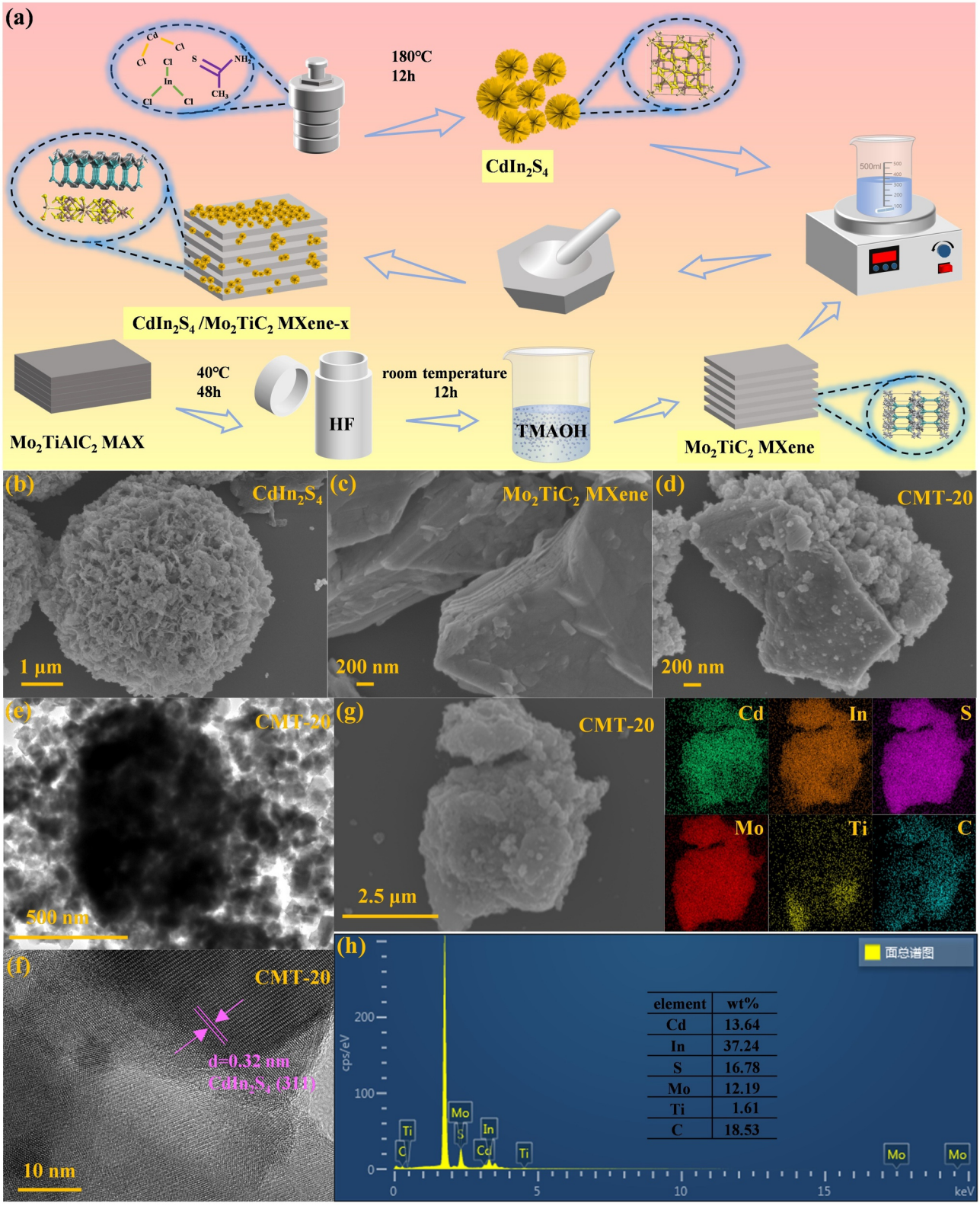

FIGURE 1 | (a) Schematic illustration of the material synthesis process; (b–d) SEM images of $CdIn_2S_4$, Mo_2TiC_2 MXene, and CMT-20 samples, respectively; (e, f) TEM and HRTEM images of CMT-20; (g) EDS elemental mapping and (h) elemental mass percentage chart of CMT-20.

2.4 | Light-Driven H_2 Evolution Experiment

The PHE experiment was conducted in a 60 mL sealed glass reactor. The specific procedure was as follows: 10 mg of catalyst sample was added to a reactor containing 30 mL of lactic acid solution (LA, 10% vol). After sealing, the mixture was subjected to ultrasonic dispersion for 2 min. Before initiating illumination, high-purity nitrogen was purged through the reaction system for

3 min to ensure an oxygen-free environment. The photoreaction was carried out under illumination from a 300 W xenon lamp with continuous stirring. The amount of hydrogen produced was quantitatively analyzed every hour using a gas chromatograph (Tianmi GC00 type, TCD detector, 13X molecular sieve chromatographic column, N_2 carrier gas). The hydrogen evolution experiment is also carried out in the same way in different systems, including 10% methanol solution, 0.25 M Na_2S/0.35 M Na_2SO_3 solution, 0.1 M ascorbic acid solution (SA), and 15% triethanolamine solution (TEOA).

2.5 | Photoelectrochemical Test

5 mg of the catalyst was dispersed in 300 μL of the mixed solution (containing 30 μL of 5% Nafion solution and 270 μL of ethanol), and after ultrasonic treatment to form a uniform dispersion solution, it was coated on a 1 × 2 cm^2 ITO conductive glass as the working electrode. In a 0.2 M Na_2SO_4 electrolyte, a three-electrode system (a platinum electrode as the counter electrode and a saturated calomel electrode as the reference electrode) was used, and the photoelectrochemical performance was tested using an electrochemical workstation (AMETEK VersaSTAT4-400) and a 300 W xenon light source.

2.6 | Materials Characterization

The surface morphology and microstructure of the samples were analyzed using scanning electron microscopy (SEM, ZEISS SIGMA 500) and transmission electron microscopy (TEM, Talos F200S). The crystal phase and chemical composition were examined by x-ray diffraction (XRD, Rigaku INTT-2000) and x-ray photoelectron spectroscopy (XPS, Thermo Fisher K-ALPHA). The optical properties of the materials were investigated via ultraviolet-visible diffuse reflectance spectroscopy (UV–Vis DRS, PerkinElmer Lambda 750) and photoluminescence/time-resolved photoluminescence spectroscopy (PL/TRPL, Fluoromax-4). Electrochemical performance tests were carried out on a VersaSTAT4-400 workstation, including photocurrent response, linear sweep voltammetry (LSV), electrochemical impedance spectroscopy (EIS), Tafel plots, and Mott–Schottky (M-S) measurements.

2.7 | Density Functional Theory Calculation

Based on the CASTEP module in Materials Studio software, first-principles calculations were performed to analyze electronic structure properties such as band structure, density of states, and work function. The Perdew–Burke–Ernzerhof (PBE) functional under the generalized gradient approximation was employed to describe the exchange-correlation interactions, with a plane-wave cutoff energy set at 400 eV. For the k-point grid, a 9 × 9 × 2 grid was selected for the $CdIn_2S_4$ system, whereas a 2 × 2 × 2 grid was adopted for the Mo_2TiC_2 MXene system.

3 | Results and Discussion

3.1 | Structural and Morphological Analysis

Figure 1a shows the preparation process of each material. Firstly, the aluminum layer in the Mo_2TiAlC_2 MAX phase was selectively etched by a hydrofluoric acid aqueous solution to successfully prepare multi-layer Mo_2TiC_2 MXene. Then, spherical $CdIn_2S_4$ was synthesized by the hydrothermal method. Finally, a binary composite material of $CdIn_2S_4$/Mo_2TiC_2 MXene with a tightly bound structure was obtained through physical stirring and grinding processes. The morphology and microstructure of $CdIn_2S_4$, Mo_2TiC_2 MXene, and CMT-20 heterojunction composite materials were systematically characterized using SEM, TEM, and HRTEM [27]. As shown in Figure 1b, the pure phase $CdIn_2S_4$ exhibits a typical flower-like spherical structure. Figure 1c indicates that after etching and layering treatment, the obtained Mo_2TiC_2 MXene presents a large area layered morphology. In the CMT-20 composite material (Figure 1d), the $CdIn_2S_4$ nanoflower balls grow on the surface of the Mo_2TiC_2 MXene nanolayers, forming a closely integrated structure. This intimate interface contact facilitates shorter charge transfer distances and enhances charge transfer efficiency [28]. The TEM images of CMT-20 further confirmed that the $CdIn_2S_4$ flower-like particles were successfully loaded on the surface of Mo_2TiC_2 MXene (Figure 1e). Since the $CdIn_2S_4$ flower-like particles completely covered the Mo_2TiC_2 MXene, in the HRTEM image of CMT-20 (Figure 1f), only the 0.32 nm lattice fringes corresponding to the (311) crystal plane of $CdIn_2S_4$ could be observed, whereas no lattice fringes of Mo_2TiC_2 MXene were detected. To probe the elemental composition and distribution of CMT-20, energy-dispersive x-ray spectroscopy (EDS) mapping was performed. Figure 1g illustrates the elemental mapping of Cd, In, S, Mo, Ti, and C. Each element is indicated by a different color, and its outline closely matches the morphology of the sample, confirming the successful preparation of the binary composite material. Figure 1h further lists the mass percentages of each element in CMT-20, with the notably low Ti content in agreement with the elemental mapping results.

The phase composition and crystal structure of $CdIn_2S_4$, Mo_2TiC_2 MXene and $CdIn_2S_4$/Mo_2TiC_2 MXene were further analyzed using XRD patterns [29]. As shown in the Figure 2a, the $CdIn_2S_4$ sample exhibits distinct diffraction peaks at 2θ values of 14.13°, 23.26°, 27.37°, 28.63°, 33.15°, 40.77°, 43.45°, and 47.55°. These peaks are indexed to the (111), (220), (311), (222), (400), (422), (511), and (440) crystal planes, respectively, confirming the cubic phase (PDF#27–0060) [30]. These results confirm that the synthesized sample is pure cubic-phase $CdIn_2S_4$ with good crystallinity. The Mo_2TiC_2 MXene (Figure 2b) was successfully synthesized by etching the Mo_2TiAlC_2 MAX phase with hydrofluoric acid (HF). The original Mo_2TiAlC_2 MAX phase exhibited main diffraction peaks at 2θ values of 9.43°, 18.99°, and 28.61°, indexed to the (002), (004), and (006) crystal planes, respectively [31]. In the XRD pattern of the resulting Mo_2TiC_2 MXene, these characteristic peaks shifted significantly to lower angles, appearing at approximately 6.83°, 13.71°, and 20.63°. This shift signifies the successful etching of

the Al layer, accompanied by a structural transition from a closely packed three-dimensional (3D) MAX phase to a two-dimensional (2D) MXene composed of nanosheets stacked via weak van der Waals forces [32]. The introduction of surface terminal groups (−O, −F, −OH) and the intercalation of water molecules collectively contributed to a significant expansion of the interlayer spacing (d_{002}) in the MXene. Figure 2c shows the XRD pattern of the $CdIn_2S_4/Mo_2TiC_2$ MXene binary heterojunction. When the loading amount of MXene is low, the diffraction pattern of the composite is largely consistent with that of pure $CdIn_2S_4$, and no distinct diffraction peaks corresponding to Mo_2TiC_2 MXene are observed, likely due to its low content and weak diffraction signal. When the content of Mo_2TiC_2 MXene increases to more than 10%, a clear weak diffraction peak emerges at $2\theta = 18.99°$, confirming the successful formation of the composite between $CdIn_2S_4$ and Mo_2TiC_2 MXene.

The chemical composition, oxidation states, and local chemical environments of relevant elements on the photocatalyst surface were systematically investigated by XPS [33]. It should be noted that all high-resolution XPS spectra were calibrated using the C 1s standard peak (284.80 eV) for binding energy correction [34]. In the high-resolution Cd 3d spectrum of pure $CdIn_2S_4$ (Figure 2d), two characteristic peaks are observed: one at a binding energy of 405.16 eV, assigned to the Cd $3d_{5/2}$ orbital, and another at 411.90 eV, corresponding to the Cd $3d_{3/2}$ orbital. These features collectively confirm the presence of Cd^{2+} [35]. Figure 2e displays the In 3d spectrum, which exhibits a well-defined doublet with peaks located at 444.76 eV (In $3d_{5/2}$) and 452.30 eV (In $3d_{3/2}$), indicating that the In element exists in the form of In^{3+} in $CdIn_2S_4$ [36]. Meanwhile, the high-resolution S 2p spectrum (Figure 2f) shows two distinct peaks at 161.42 and 162.66 eV, which are attributed to the S $2p_{3/2}$ and S $2p_{1/2}$ spin–orbit components, respectively, further verifying the existence of S^{2-} [37]. For the pristine Mo_2TiC_2 MXene material, the C 1s XPS spectrum (Figure 2g) can be deconvoluted into four components with binding energies at 282.97 eV, 284.80 eV, 286.04 eV, and 288.68 eV, corresponding to C-Ti/Mo, C-C/C=C, C-O, and C=O bonds, respectively [38]. The Mo 3d high-

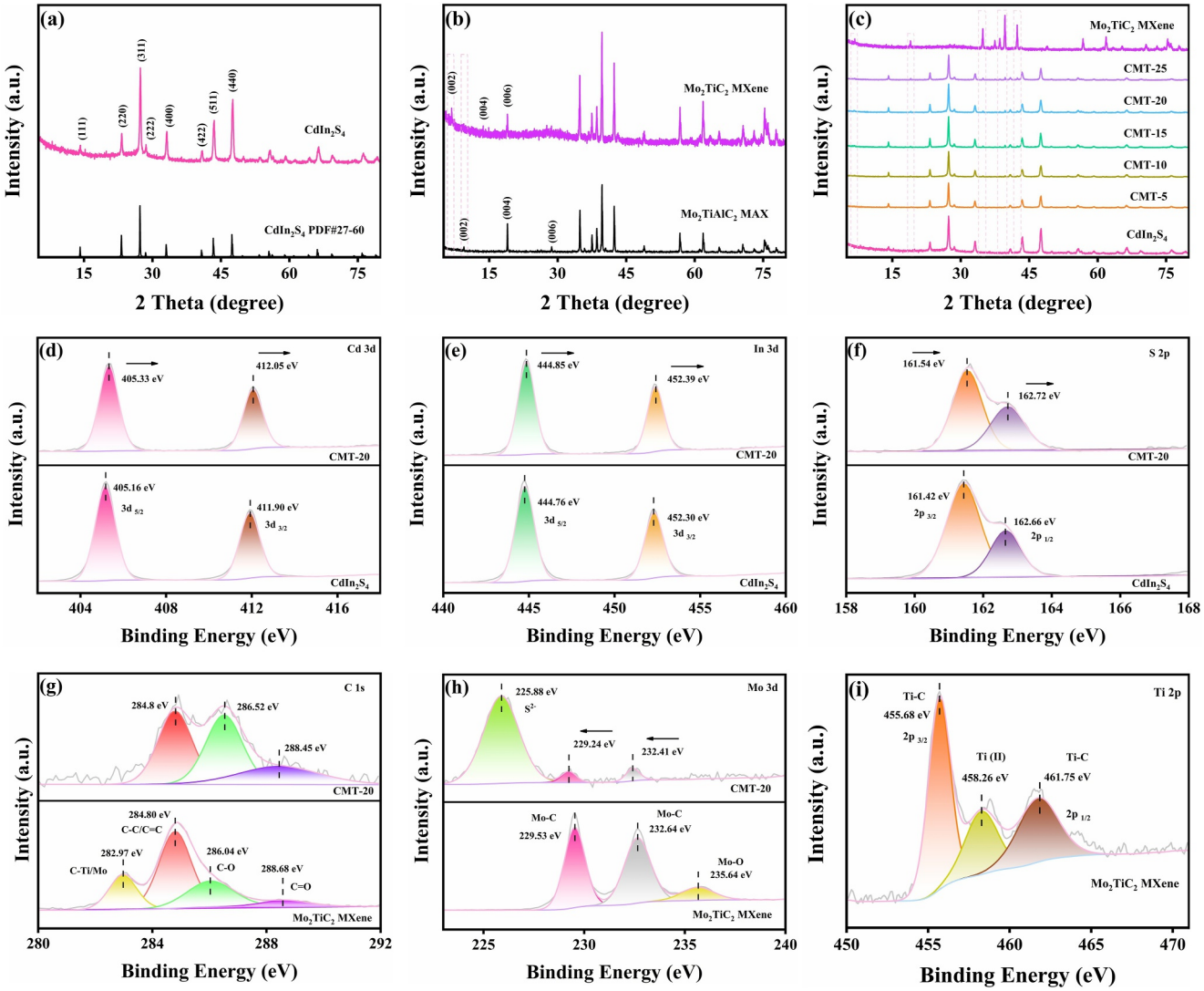

FIGURE 2 | (a–c) XRD patterns of $CdIn_2S_4$, Mo_2TiC_2 MXene, and composite catalyst CMT-x; (d–i) High-resolution XPS spectra of the corresponding samples: (d–f) Cd 3d, In 3d, and S 2p spectra for $CdIn_2S_4$ and CMT-20; (g, h) C 1s and Mo 3d spectra for Mo_2TiC_2 MXene and CMT-20; (i) Ti 2p spectrum for Mo_2TiC_2 MXene.

resolution spectrum (Figure 2h) exhibits three characteristic peaks: those at 229.53 and 232.64 eV are assigned to the Mo-C bond in the $3d_{5/2}$ and $3d_{3/2}$ states, respectively, whereas the peak at 235.64 eV is attributed to the Mo-O bond ($3d_{3/2}$) [39]. Furthermore, the Ti 2p spectrum (Figure 2i) displays two peaks at 455.68 and 461.75 eV, which are assigned to Ti-C bonds, along with an additional peak at 458.26 eV corresponding to Ti(II) species [40]. The presence of the C-Ti/Mo peak at 282.97 eV in the C 1s spectrum is consistent with the metal-carbon signals observed in both the Mo 3d and Ti 2p spectra, collectively confirming the successful synthesis and formation of the ternary carbide Mo_2TiC_2 MXene. The absence of a C-Ti/Mo peak in the C 1s spectrum of CMT-20 (Figure 2g) is likely due to the low Ti content in the composite. In the high-resolution spectrum of Mo 3d, the peak at a binding energy of 225.88 eV should be assigned to S 2s, originating from the $CdIn_2S_4$ component present in CMT-20 (Figure 2h) [41]. Additionally, the relative intensity of the high-resolution Mo 3d signal in CMT-20 is significantly lower than that in Mo_2TiC_2 MXene, and no high-resolution Ti 2p signal was detected. This is likely due to the complete encapsulation of Mo_2TiC_2 MXene nanosheets by $CdIn_2S_4$ and the relatively low overall addition amount of Mo_2TiC_2 MXene. To support the XPS analysis results, inductively coupled plasma optical emission spectrometry (ICP-OES) was further employed to determine the actual content of metallic elements in CMT-20 [42]. The results showed that the contents of Cd, In, Mo, and Ti were 21.63%, 38.04%, 11.31%, and 2.96% (Table 1), respectively, indicating the successful formation of a composite between $CdIn_2S_4$ and Mo_2TiC_2 MXene. XPS analysis can also be employed to study the charge transfer behavior between catalysts [43]. The changes in binding energy reflect alterations in electron cloud density: in the composite material, the binding energies of the Cd 3d, In 3d, and S 2p orbitals all increased, whereas that of Mo 3d decreased. This phenomenon arises from the interfacial coupling and strong electronic interaction between $CdIn_2S_4$ and Mo_2TiC_2 MXene, indicating that electrons are transferred from $CdIn_2S_4$ to Mo_2TiC_2 MXene, which further confirms the successful construction of a heterojunction between the two materials [44].

TABLE 1 | Elemental analysis results of CMT-20 by ICP-OES analysis (wt%).

Sample	Cd	In	Mo	Ti
CMT-20	21.63	38.04	11.31	2.96

3.2 | Photocatalytic Performance Assessment

The PHE performance of $CdIn_2S_4/Mo_2TiC_2$ MXene composite materials and their individual components was evaluated under 300 W xenon lamp irradiation, using lactic acid (LA) as the hole scavenger. As shown in Figure 3a, pure Mo_2TiC_2 MXene and $CdIn_2S_4$ exhibit relatively low hydrogen production rates due to the rapid recombination rate of photogenerated carriers. It is notable that the composite material $CdIn_2S_4/Mo_2TiC_2$ MXene (CMT-20) with a mass ratio of 20% demonstrates the optimal PHE activity. Its hydrogen production rate reaches 3.35 $mmol \cdot h^{-1}\ g^{-1}$, which is 3350 times and 55.83 times higher than that of pure Mo_2TiC_2 MXene and $CdIn_2S_4$, respectively. This significant improvement can be attributed to the charge redistribution effect induced by the Schottky heterojunction, which promotes electron enrichment on the surface of Mo_2TiC_2 MXene, thereby enhancing the catalytic activity [45, 46]. When

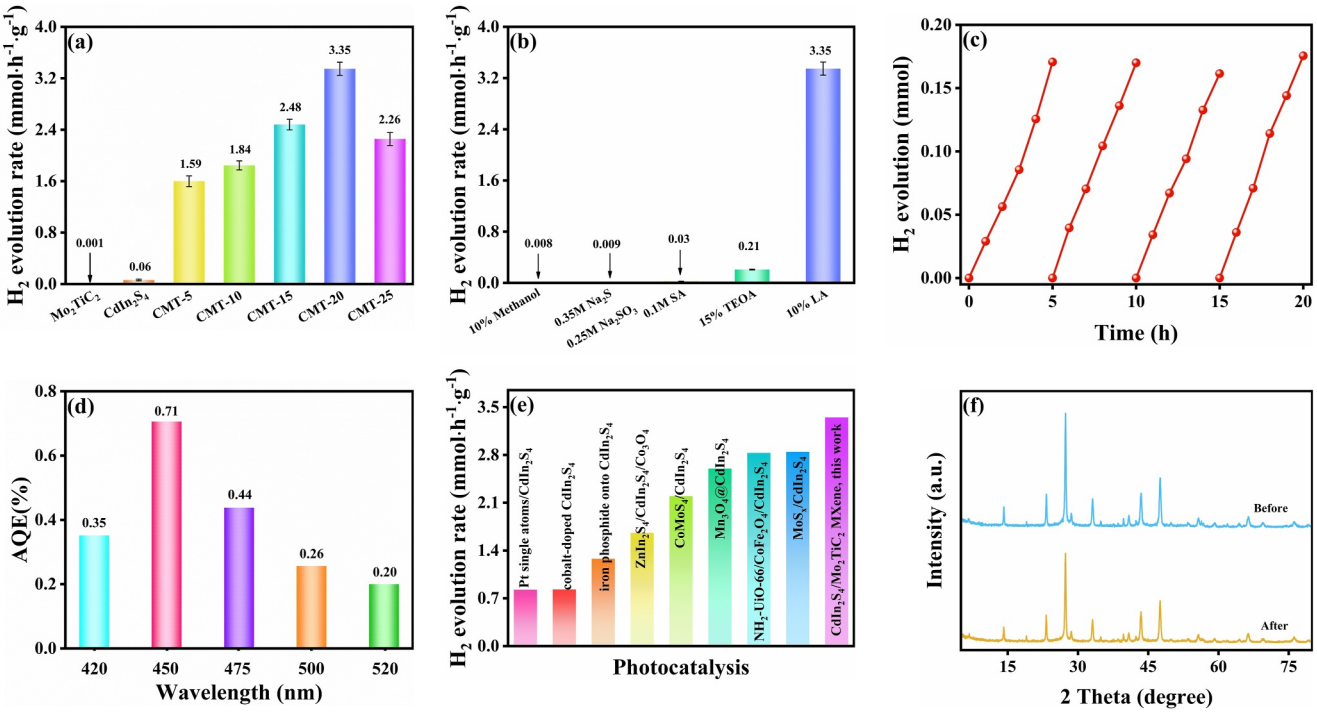

FIGURE 3 | (a) Comparison of PHE rates among Mo_2TiC_2 MXene, $CdIn_2S_4$ and CMT-x composites; (b) Evaluation of PHE performance for CMT-20 using different sacrificial reagents; (c) Cyclic stability test of CMT-20 over 20 h of PHE; (d) Measured AQE values for CMT-20 at different wavelengths; (e) Performance comparison of various $CdIn_2S_4$-based photocatalysts; (f) XRD patterns of CMT-20 before and after PHE.

the mass ratio of Mo_2TiC_2 MXene exceeds 20%, the PHE performance decreases. This is mainly due to the excessive Mo_2TiC_2 MXene generating a "shielding effect", which weakens the light absorption ability of the $CdIn_2S_4$ semiconductor [47, 48]. On the contrary, when the content of Mo_2TiC_2 MXene is lower than 20%, the hydrogen production activity also decreases. This may be because the insufficient Mo_2TiC_2 MXene content leads to a reduction in the heterojunction interface and insufficient electron transmission channels, thereby reducing the carrier separation efficiency [49, 50]; at the same time, the insufficient active sites also limit the ability of photogenerated electrons to participate in the reduction reaction, thereby inhibiting the generation of hydrogen [51, 52]. As shown in Figure 3b, under different sacrificial reagent conditions, the order of the rates of H_2 production by photocatalysis is: LA > TEOA > SA > Na_2S/Na_2SO_3 > methanol. When using sacrificial reagents other than lactic acid, the photogenerated holes cannot be effectively consumed, thus more easily recombine with photogenerated electrons, making it difficult for effective hydrogen gas release active sites to form on the surface of the photocatalyst, and thereby inhibiting the overall photocatalytic reaction [53, 54]. Furthermore, the CMT-20 catalyst exhibits excellent stability. During four consecutive cycling experiments, its photocatalytic activity did not show any significant decline, indicating that this material has good durability in solar-driven hydrogen production (Figure 3c) [55]. As illustrated in Figure 3d, the apparent quantum yield (AQE) of CMT-20 at wavelengths of 420, 450, 475, 500, and 520 nm was 0.35%, 0.71%, 0.44%, 0.26%, and 0.20% respectively, indicating that this catalyst can effectively utilize visible light to achieve hydrogen production through photocatalysis. It is worth noting that the hydrogen generation rate of CMT-20 reached 3.35 $mmol \cdot h^{-1}\ g^{-1}$, which was superior to most of the previously reported photocatalysts based on $CdIn_2S_4$ (Figure 3e, Table 2). The XRD test conducted 20 h after the reaction showed that the crystal structure of the CMT-20 composite material did not undergo any significant changes, further confirming its excellent photostability (Figure 3f) [56].

3.3 | Optical and Band Structure Properties

The UV–vis DRS results are shown in Figure 4a. Mo_2TiC_2 MXene exhibits significant light absorption capability throughout the visible light range. The optical absorption range of $CdIn_2S_4$ is wide, with its absorption edge extending to 600 nm. The composite catalyst CMT-20 prepared by introducing an appropriate amount of Mo_2TiC_2 MXene into $CdIn_2S_4$ has significantly enhanced light absorption capability in the entire visible light region compared to pure $CdIn_2S_4$ [57]. This is mainly attributed to the strong light capture ability of Mo_2TiC_2 MXene in the visible light range, which forms a synergistic effect with $CdIn_2S_4$, thereby significantly enhancing the light

TABLE 2 | Comparative hydrogen production rates of various $CdIn_2S_4$-based photocatalysts.

Serial number	Photocatalyst	HER ($mmol \cdot g^{-1}\ h^{-1}$)	Sacrificial reagent	Light source	Pub date	Ref
1	Pt single atoms/$CdIn_2S_4$	0.82	10 vol% TEOA	300 W Xe lamp (λ > 420 nm)	2025-06-06	Chemical engineering journal 517 (2025) 164289
2	Cobalt-doped $CdIn_2S_4$	0.83	20 vol% methanol solution	500 W Xe lamp (λ > 420 nm)	2025-01-26	Journal of colloid and interface science 685 (2025) 1122–1130
3	Iron phosphide/ $CdIn_2S_4$	1.28	10 vol% lactic acid	300 W Xe lamp (λ > 400 nm)	2025-04-15	Inorganic chemistry communications 178 (2025) 114552
4	$ZnIn_2S_4$/ $CdIn_2S_4$/ Co_3O_4	1.66	7 mL $KHCO_3$ (aq) (0.5 M), 5 mL TEOA, and 10 mL CH_3CN	300 W Xe lamp (λ > 400 nm)	2024-04-10	Surfaces and interfaces 48 (2024) 104342
5	$CoMoS_4$/ $CdIn_2S_4$	2.19	10 vol% TEOA	300 W Xe lamp (λ > 420 nm)	2023-08-25	International journal of hydrogen energy 51 (2024) 133–144
6	Mn_3O_4/ $CdIn_2S_4$	2.6	0.35 M Na_2S/0.25M Na_2SO_3	300 W Xe lamp	2024-03-12	Separation and purification technology 343 (2024) 127091
7	NH_2-UiO-66/ $CoFe_2O_4$/ $CdIn_2S_4$	2.83	20 vol% TEOA	300 W Xe lamp (λ > 420 nm)	2022-01-19	Chemical engineering journal 435 (2022) 134740
8	MoSx/$CdIn_2S_4$	2.84	0.1 M Na_2S/Na_2SO_3	300 W Xe lamp	2020-12-14	Catalyst 10 (2020) 1455
9	This work $CdIn_2S_4$/ MXene	3.35	10 vol% lactic acid aqueous	300 W Xe lamp	—	—

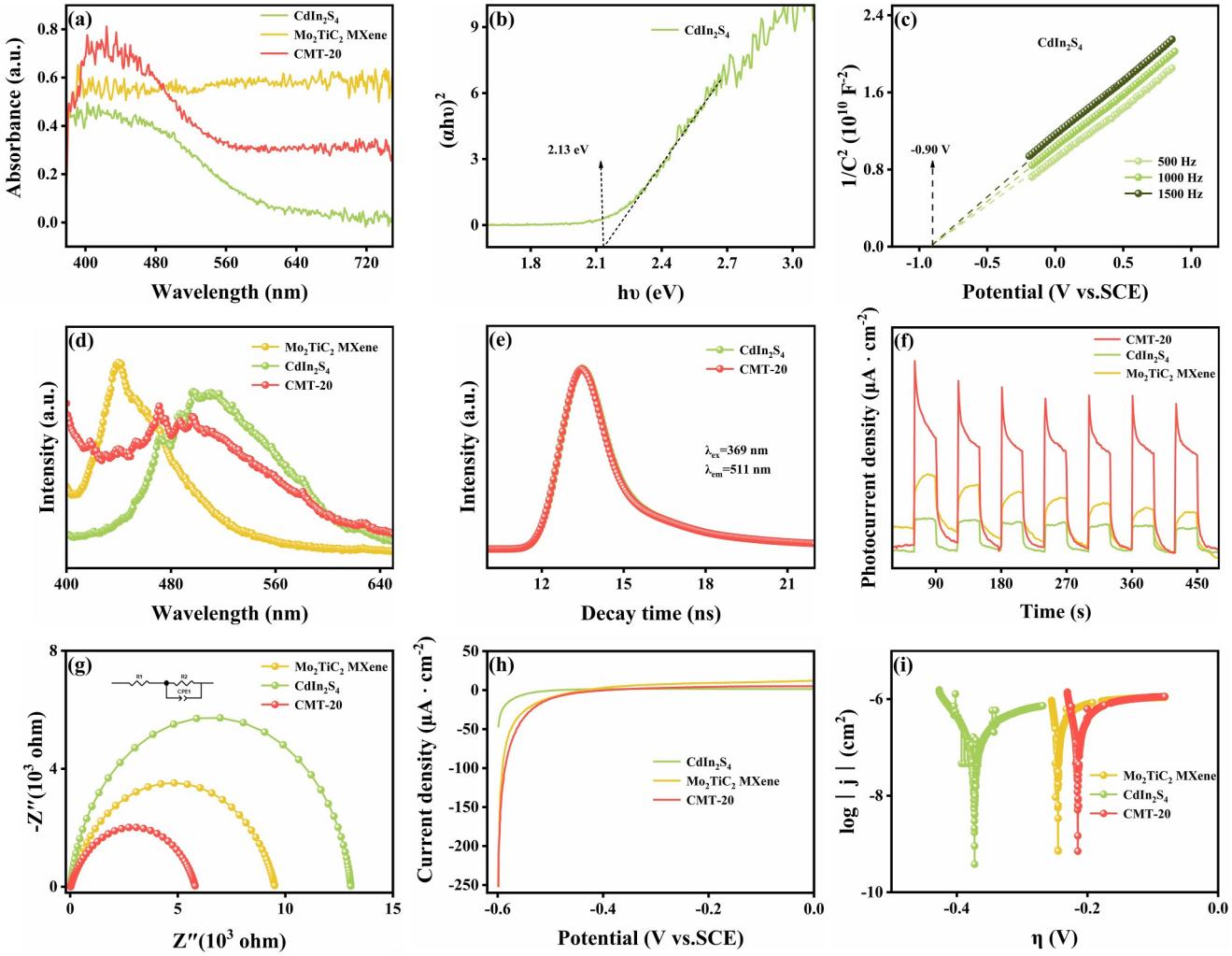

FIGURE 4 | (a) The UV–vis DRS of Mo_2TiC_2 MXene, $CdIn_2S_4$ and CMT-20; (b) Band gap diagram of $CdIn_2S_4$; (c) M-S curves of $CdIn_2S_4$ at different frequencies; (d) The PL spectra of Mo_2TiC_2 MXene, $CdIn_2S_4$ and CMT-20; (e) The TPPL spectra of $CdIn_2S_4$ and CMT-20; (f) Transient photocurrent responses, (g) EIS Nyquist plots, (h) LSV, (i) Tafel of Mo_2TiC_2 MXene, $CdIn_2S_4$ and CMT-20.

absorption intensity of the composite material. To further evaluate the band gap energy of $CdIn_2S_4$, a Tauc plot was drawn based on the UV–vis DRS data [58]. By extrapolating the linear part of the $(\alpha h\nu)^2$ versus photon energy ($h\nu$) relationship curve to the *x*-axis (Figure 4b), the bandgap energy of $CdIn_2S_4$ is approximately 2.13 eV. This band gap value indicates that $CdIn_2S_4$ has good visible light absorption capability and is suitable for visible light-driven photocatalytic reactions. The Mottle-Schottky (M-S) test results (Figure 4c) indicate that $CdIn_2S_4$ is an n-type semiconductor, and its M-S curve shows a positive slope [59]. The flat band potential of the material relative to the saturated calomel electrode (SCE) was measured to be −0.90 V, and the corresponding conduction band potential (E_{CB}) (vs. SCE) was −1.1 V. Since the E_{CB} of n-type semiconductors relative to the standard hydrogen electrode (NHE) is typically 0.24V positive than that relative to SCE, the CB position of $CdIn_2S_4$ (vs. NHE) is −0.86V. Based on the bandgap values shown in Figure 4b, the valence band position (E_{VB}) of $CdIn_2S_4$ can be further calculated as 1.27 V (vs. NHE).

3.4 | Photoinduced Charge Transfer Efficiency

Photoluminescence (PL) spectroscopy can be used to evaluate the separation efficiency of photogenerated carriers in photocatalytic materials. The basis for this is that when a semiconductor is excited by light, the electron-hole pairs produced will release fluorescence when they undergo radiative recombination [60]. The intensity of the PL signal directly reflects the recombination probability of photogenerated carriers. Therefore, a lower PL intensity usually indicates more effective charge separation [61]. Under 380 nm excitation, the PL emission spectrum shows that the emission peak of Mo_2TiC_2 MXene is at 440 nm, and that of $CdIn_2S_4$ is at 510 nm (Figure 4d). However, the CMT-20 composite catalyst shows a distinct emission peak at 500 nm, but its peak position has undergone a blue shift of approximately 10 nm compared to pure $CdIn_2S_4$ (510 nm) [62, 63]. The overall PL strength of the CMT-20 complex was significantly weakened compared with that of a single component. This strongly demonstrates that the introduction of

TABLE 3 | Kinetic analysis of emission decay for $CdIn_2S_4$ and CMT-20 samples.

Sample	Lifetime, τ (ns)	Rel (%)	$\langle\tau\rangle$ (ns)	χ^2
$CdIn_2S_4$	$\tau_1 = 3.85$	$A_1 = 22.41$	1.19	1.43
	$\tau_2 = 150.93$	$A_2 = 25.79$		
	$\tau_3 = 0.66$	$A_3 = 51.80$		
CMT-20	$\tau_1 = 3.74$	$A_1 = 23.83$	1.12	1.50
	$\tau_2 = 135.29$	$A_2 = 24.27$		
	$\tau_3 = 0.63$	$A_3 = 51.90$		

Mo_2TiC_2 MXene has successfully constructed an efficient heterojunction interface, greatly promoting the spatial separation of photogenerated electron-hole pairs and suppressing their recombination within the bulk phase [64]. The time-resolved photoluminescence (TRPL) test results (Figure 4e) show that the CMT-20 composite material has the shortest average fluorescence decay lifetime (1.12 ns) (Table 3). The shorter lifetime indicates that the non-radiative recombination path of photogenerated carriers is dominant, which usually stems from the efficient interfacial charge transfer process [65]. This means that electrons and holes can be rapidly separated in CMT-20 and migrate to the surface to participate in the reaction, thereby providing crucial kinetic evidence for its significantly enhanced photocatalytic activity.

Photocurrent response tests were conducted on Mo_2TiC_2 MXene, $CdIn_2S_4$ and CMT-20 under 300W xenon lamp irradiation (Figure 4f). During the seven light-dark cycles, each catalyst exhibited repeatable photocurrent responses within each light cycle. Notably, the photocurrent density of CMT-20 was significantly higher than that of Mo_2TiC_2 MXene and $CdIn_2S_4$, reflecting its superior light capture ability and stronger photogenerated carrier separation efficiency [66]. The test results of electrochemical impedance spectroscopy (EIS) are shown in Figure 4g. Pure phase $CdIn_2S_4$ exhibits the largest Nyquist radius, which means it has the highest charge transfer resistance. In contrast, after introducing the Mo_2TiC_2 MXene to form the CMT-20 composite material, the Nyquist radius significantly decreased, indicating that the construction of the Schottky heterojunction reduced the charge transfer resistance and significantly increased the interface charge transfer rate [67, 68]. The hydrogen evolution activity of the material was evaluated by linear scanning voltammetry (LSV). As shown in Figure 4h, under the same current density, CMT-20 requires the lowest overpotential, indicating that its catalytic activity is optimal [69]. Further Tafel analysis (Figure 4i) revealed that the overpotential of CMT-20 was closest to zero, indicating that a significant increase in current density could be achieved by applying a smaller overpotential increment, revealing its faster reaction kinetics process [70].

3.5 | Density Functional Theory Calculation Analysis

The electronic structures of $CdIn_2S_4$ and Mo_2TiC_2 MXene were calculated using density functional theory (DFT), and their structural models are shown in Figure 5a,d respectively. The results of the band structure calculation (Figure 5b) indicate that $CdIn_2S_4$ is a direct bandgap semiconductor with a theoretical bandgap value of 0.97 eV. This value is lower than the experimental measurement, and this difference can be attributed to the generally underestimated bandgap effect of the generalized gradient approximation (GGA) functional [71]. Further analysis of the density of states (Figure 5c) shows that the CB of $CdIn_2S_4$ is mainly contributed by *p* and d orbitals, with a small amount of s orbitals involved; whereas the VB is mainly composed of s and *p* orbitals. In contrast, the band structure of Mo_2TiC_2 MXene does not show a band gap (Figure 5e), indicating its metal-like properties [72, 73]. This conclusion is further supported by the density of states plot (Figure 5f): the VB and CB of Mo_2TiC_2 MXene intersect at the Fermi level (E_f), and there is a broad energy band mainly contributed by d orbital electrons near the E_f, resulting in a significant electron density of states at this point and thus no formation of a band gap. Furthermore, the calculation also obtained the work functions (Φ) of the $CdIn_2S_4$ (311) crystal plane (Figure 5g) and the Mo_2TiC_2 MXene (002) crystal plane (Figure 5h), which were 4.91 and 5.19 eV respectively. The Φ reflects the minimum energy required for electrons to escape from the interior of the material to the surface. The lower the value, the easier the electrons escape [74]. The calculation results showed that the Φ of Mo_2TiC_2 MXene was higher than that of $CdIn_2S_4$. Based on the relationship E_f = Evac - Φ (where E_f is the Fermi energy level and Eac is the vacuum energy level), it was determined that the Fermi energy level of $CdIn_2S_4$ is higher than that of Mo_2TiC_2 MXene. Based on these results, the differences in the Φ and E_f between the two component materials induced the transfer of electrons from $CdIn_2S_4$ to Mo_2TiC_2 MXene, ultimately resulting in charge rearrangement within the CMT-20 composite material and achieving Fermi energy level balance at the interface [75–80]. This interface charge transfer behavior was also experimentally confirmed in the aforementioned XPS tests.

3.6 | Photocatalytic Mechanism Analysis

To clarify the charge migration mechanism in the CMT-20 heterojunction, this study combined UV–Vis DRS, Mott–Schottky tests, and band structure calculations to determine the electrical properties of $CdIn_2S_4$ and Mo_2TiC_2 MXene. The results showed that $CdIn_2S_4$ is a direct bandgap semiconductor, whereas Mo_2TiC_2 MXene exhibits metallic-like characteristics. Further, through DFT calculations, the interface structure between the $CdIn_2S_4$ (311) crystal plane and the Mo_2TiC_2 MXene (002) crystal plane was simulated. The calculation shows that the E_f of $CdIn_2S_4$ is higher than that of Mo_2TiC_2 MXene. When the two were in close contact, the difference in E_f promoted the migration of free electrons from $CdIn_2S_4$ to Mo_2TiC_2 MXene until the E_f of the system reached equilibrium. This conclusion was also supported by XPS characterization.

Based on the above analysis, this study proposes the charge transfer mechanism at the CMT-20 Schottky heterojunction interface, as shown in Figure 5i. Before contact, the E_f of $CdIn_2S_4$ is significantly higher than that of Mo_2TiC_2 MXene. After contact, under light illumination, $CdIn_2S_4$ is excited and

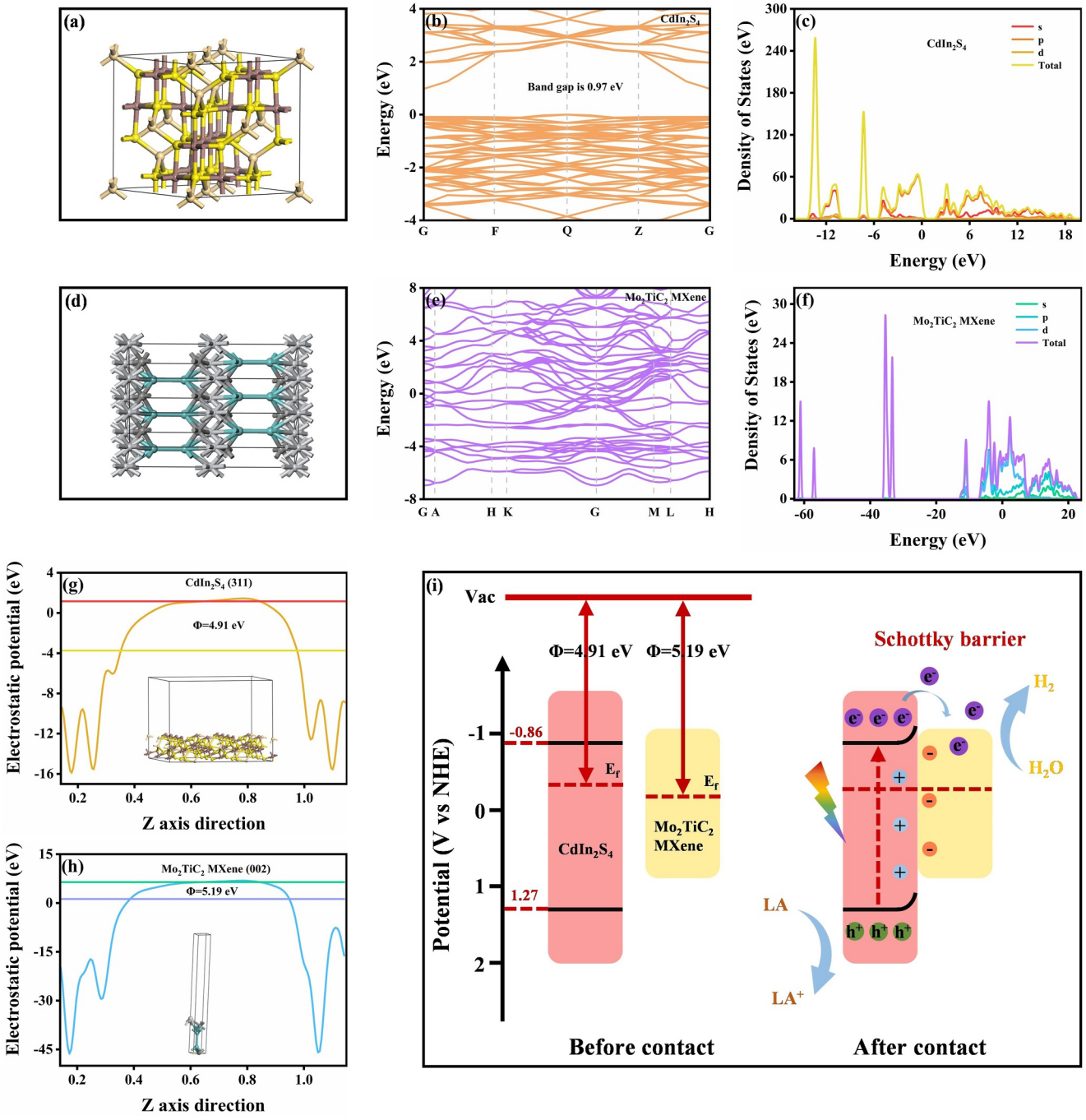

FIGURE 5 | (a, d) Computed geometric structures of $CdIn_2S_4$ and Mo_2TiC_2 MXene; (b, c, g) Calculated band gap, density of states, and work function corresponding to $CdIn_2S_4$; (e, f, h) Calculated band gap, density of states, and work function corresponding to Mo_2TiC_2 MXene; (i) Proposed PHE mechanism for the $CdIn_2S_4/Mo_2TiC_2$ MXene composite.

generates photogenerated electron-hole pairs. Due to the difference in E_f between the two, electrons spontaneously migrate from $CdIn_2S_4$ to Mo_2TiC_2 MXene until the system reaches charge equilibrium, forming a Schottky barrier and causing band bending. The photogenerated electrons are captured by the Mo_2TiC_2 MXene with metallic conductivity, which rapidly transfers to the reaction interface due to its high conductivity, thereby providing abundant catalytic active sites. Meanwhile, the formed band bending and Schottky barrier promote the electron to migrate unidirectionally from $CdIn_2S_4$ to Mo_2TiC_2 MXene, effectively preventing the reverse flow of electrons and enhancing the separation efficiency of photogenerated carriers. Additionally, the addition of lactic acid (LA) as a sacrificial agent in the system can promptly consume the residual holes in $CdIn_2S_4$, generating the oxidized LA^+, further inhibiting the recombination of electron-hole pairs.

4 | Conclusion

$CdIn_2S_4/Mo_2TiC_2$ MXene composite photocatalyst was successfully prepared through combined physical stirring and

grinding. Experimental results demonstrate that the introduction of Mo_2TiC_2 MXene significantly enhances both the PHE activity and stability of the composite. The CMT-20 sample exhibits optimal performance, achieving a hydrogen production rate of 3.35 mmol·h^{-1} g^{-1}, which is 55.83 times higher than that of pure $CdIn_2S_4$. Based on photoelectrochemical tests and theoretical calculations, a Schottky heterojunction is formed between $CdIn_2S_4$ and Mo_2TiC_2 MXene, establishing efficient charge transfer channels that promote the separation of photogenerated carriers and consequently enhance the PHE performance. This study verifies the feasibility of Mo_2TiC_2 MXene as a non-noble metal co-catalyst for PHE and provides new insights for developing clean energy technologies based on the unique physicochemical properties of MXene materials.

Author Contributions

Bingzhu Li: conceptualization, methodology, investigation, writing – original draft. **Teng Li:** conceptualization, methodology, investigation, writing – original draft. **Minjun Lei:** validation. **Noritatsu Tsubaki:** validation. **Xiaohua Ma:** writing – review and editing, supervision. **Zhiliang Jin:** funding acquisition, project administration. **Paolo Fornasiero:** funding acquisition, project administration.

Acknowledgments

The authors acknowledge the Natural Science Foundation of Ningxia (2021AAC03194) for financial support.

Conflicts of Interest

The authors declare no conflicts of interest.

Data Availability Statement

The data that support the findings of this study are available from the corresponding author upon reasonable request.

References

1. X. Miao, H. Yang, J. He, J. Wang, and Z. Jin, "Adjusting the Electronic Structure of Keggin-Type Polyoxometalates to Construct S-Scheme Heterojunction for Efficient Photocatalytic Hydrogen Evolution," *Acta Physico-Chimica Sinica* 41, no. 6 (2025): 100051, https://doi.org/10.1016/j.actphy.2025.100051.

2. Q. Ma, J. Wei, Z. Lin, et al., "Enhanced Photocatalytic Performance of Ce^{3+}-doped $ZnIn_2S_4$ Through Vacancy Engineering for Efficient Hydrogen Evolution and Pollutant Degradation," *Applied Catalysis B: Environment and Energy* 378 (2025): 125547, https://doi.org/10.1016/j.apcatb.2025.125547.

3. R. Liu, X. Zhang, X. Han, Y. Sun, S. Jin, and R. Liu, "Photocatalytic Degradation of Tetracycline With Fe_3O_4/g-C_3N_4/TiO_2 Catalyst Under Visible Light," *Carbon Letters* 34, no. 1 (2024): 75–83, https://doi.org/10.1007/s42823-023-00661-6.

4. R. Li, C. Zhang, K. You, et al., "Molecular Confined Synthesis of Magnetic CoO_x/Co/C Hybrid Catalyst for Photocatalytic Water Oxidation and CO_2 Reduction," *Chinese Chemical Letters* 34, no. 12 (2023): 108801, https://doi.org/10.1016/j.cclet.2023.108801.

5. J. Du, F. Jin, Y. Li, G. Jiang, and Z. Jin, "In-Situ Mo Doping in NiS_2: Enhancing Electron Density and Stimulating Electronic Conductivity of Cu_3P-GDY for Efficient Photocatalytic Hydrogen Evolution," *Journal of Materials Chemistry A* 13, no. 7 (2025): 4994–5006, https://doi.org/10.1039/d4ta07562e.

6. G. Ding, Z. Wang, J. Zhang, P. Wang, L. Chen, and G. Liao, "Layered Double Hydroxides-Based Z-Scheme Heterojunction for Photocatalysis," *EcoEnergy* 2, no. 1 (2024): 22–44, https://doi.org/10.1002/ece2.25.

7. C. Zhuang, A. Zhang, Y. Zhang, et al., "Photocatalytic Cocatalysts: Classification, Structural Design and Crucial Role in Various Reactions," *Coordination Chemistry Reviews* 542 (2025): 216867, https://doi.org/10.1016/j.ccr.2025.216867.

8. Z. Zhou and Z. Jin, "Custom Exposed Crystal Facets: Synergistic Effect of Optimum Crystal Facet Anisotropy and Ohmic Heterojunction Boosting Photocatalytic Hydrogen Evolution," *Chinese Journal of Catalysis* 74 (2025): 294–307, https://doi.org/10.1016/s1872-2067(25)64690-0.

9. L. Ding, M. Lei, T. Wang, J. Wang, and Z. Jin, "Graphdiyne Coordinated CoMo-MOF Formed S-Scheme Heterojunction Boosting Photocatalytic Hydrogen Production," *Carbon Letters* 34, no. 8 (2024): 2099–2112, https://doi.org/10.1007/s42823-024-00743-z.

10. T. Tian, W. Wang, Y. Wang, et al., "Mo-Doping and CoO_x Loading Over $BiVO_4$ Photoanode for Enhancing Performance of H_2O_2 Synthesis and in-Situ Organic Pollutant Degradation," *Chinese Journal of Catalysis* 67 (2024): 176–185, https://doi.org/10.1016/s1872-2067(24)60175-0.

11. H. Yang, Y. Zhao, K. Huang, and X. Meng, "Photothermally Catalytic Fixation of N_2 over TiO_2 Loaded Onto Carbon Paper by Fast Joule Heating," *Rare Metals* 44, no. 5 (2025): 3206–3217, https://doi.org/10.1007/s12598-024-03066-0.

12. F. Cui, Q. Zhang, T. Xiao, Z. Wang, and L. Wang, "Photocaged Activity-Based Probes for Improved Monitoring of Protein S-Sulfenylation in Living Cells," *Chinese Chemical Letters* 35, no. 10 (2024): 110061, https://doi.org/10.1016/j.cclet.2024.110061.

13. Q. Zhang, Y. Chu, Z. Liu, et al., "Construction of Triazine-Heptazine-Based Carbon Nitride Heterojunctions Boosts the Selective Photocatalytic C-C Bond Cleavage of Lignin Models," *Applied Catalysis B: Environmental* 331 (2023): 122688, https://doi.org/10.1016/j.apcatb.2023.122688.

14. J. Ma, A. Li, Q. Liu, L. Chen, M. Hong, and R. Sun, "Efficient Production of Syngas and Lactic Acid via CrB MBene/$Cd_{0.8}Zn_{0.2}S$ Schottky Heterojunction Photocatalysis," *Applied Catalysis B: Environment and Energy* 367 (2025): 125101, https://doi.org/10.1016/j.apcatb.2025.125101.

15. Z. Zhou, H. Yao, Y. Wu, T. Li, N. Tsubaki, and Z. Jin, "Synergistic Effect of Cu-Graphdiyne (C_nH_{2n-2})/transition Bimetallic Tungstate Formed S-Scheme Heterojunction for Enhanced Photocatalytic Hydrogen Evolution," *Acta Physico-Chimica Sinica* 40, no. 10 (2024): 2312010, https://doi.org/10.3866/pku.whxb202312010.

16. J. Deng, J. Liang, Z. Hu, et al., "Schottky Heterojunctions Enabled by Covalent Organic Frameworks and Copper Electron Sponge for Boosting Photocatalytic Hydrogen Evolution," *Applied Catalysis B: Environment and Energy* 378 (2025): 125593, https://doi.org/10.1016/j.apcatb.2025.125593.

17. S. Sambyal, A. Sudhaik, S. Sonu, et al., "Recent Updates on Cadmium Indium Sulfide ($CdIn_2S_4$ or CIS) Photo-Catalyst: Synthesis, Enhancement Strategies and Applications," *Coordination Chemistry Reviews* 535 (2025): 216653, https://doi.org/10.1016/j.ccr.2025.216653.

18. J. Teng, F. Li, T. Li, M. Huttula, and W. Cao, "Enhanced Visible Light-Driven Hydrogen Evolution in Non-Precious Metal Ni_2P/$CdIn_2S_4$ S-Type Heterojunction via Rapid Interfacial Charge Transfer," *Materials Today Advances* 22 (2024): 100503, https://doi.org/10.1016/j.mtadv.2024.100503.

19. W. Zhang, K. Wei, L. Fan, et al., "Core-Shell Structured Mn_3O_4@$CdIn_2S_4$ Microspheres With S-Scheme Charge Transfer Route for Efficient Photocatalytic Hydrogen Evolution," *Separation and Purification Technology* 343 (2024): 127091, https://doi.org/10.1016/j.seppur.2024.127091.

20. G. Zhang, D. Shi, Z. Wang, et al., "Purposefully Construction of $ZnIn_2S_4/CdIn_2S_4/Co_3O_4$ Synergistic Mix-Heterojunction for Enhanced CO_2 Photoconversion and H_2 Evolution Reaction via Cascade Charge Transfer," *Surfaces and Interfaces* 48 (2024): 104342, https://doi.org/10.1016/j.surfin.2024.104342.

21. Z. Kong, Z. Kong, D. Zhang, et al., "Magnetic Separable Non-Precious Metal Schottky Heterojunction Photocatalyst Toward Photothermal-Assisted Photocatalytic Hydrogen Evolution," *Separation and Purification Technology* 361 (2025): 131429, https://doi.org/10.1016/j.seppur.2025.131429.

22. L. Fan, X. Guo, L. Wang, Z. Jin, and N. Tsubaki, "Excellent Charge Separation Over $NiCo_2S_4/CoTiO_3$ Nanocomposites Improved Photocatalytic Hydrogen Production," *Frontiers of Chemical Science and Engineering* 18 (2024): 158, https://doi.org/10.1007/s11705-024-2509-y.

23. Y. Fan, X. Hao, N. Yi, and Z. Jin, "Strong Electronic Coupling of Mo_2TiC_2 MXene/ZnCdS Ohmic Junction for Boosting Photocatalytic Hydrogen Evolution," *Applied Catalysis B: Environment and Energy* 357 (2024): 124313, https://doi.org/10.1016/j.apcatb.2024.124313.

24. H. Zhang, Y. Huang, X. Wang, et al., "Tightly-Bound Interfaces Between $ZnIn_2S_4$ Nanosheets and Few-Layered Mo_2TiC_2 MXene Induced Highly Efficient Noble-Metal-Free Schottky Junction for Photocatalytic Hydrogen Evolution," *Separation and Purification Technology* 360 (2025): 131199, https://doi.org/10.1016/j.seppur.2024.131199.

25. W. Liu, C. Zhang, J. Shi, et al., "Improved Carriers Transfer Dynamics Through Dual-Functional Charge Trapping and Electronic Tailoring for Photocatalytic Hydrogen Production," *Applied Catalysis B: Environment and Energy* 381 (2026): 125858, https://doi.org/10.1016/j.apcatb.2025.125858.

26. X. Guo, J. Liu, X. Yang, Z. Jin, and N. Tsubaki, "Construction of ZnCdSe/Triazine-Graphdiyne S-Scheme Heterojunction for Boosting Photocatalytic Hydrogen Evolution," *Chemical Research in Chinese Universities* 41, no. 4 (2025): 893–902, https://doi.org/10.1007/s40242-025-5125-6.

27. Y. Wu, H. Wang, and Z. Jin, "Development and Application of the Synthesis of Graphdiyne by One–Pot Conjugation," *Journal of Ningxia University (Natural Science Edition)* 45 (2024): 361–371, https://doi.org/10.20176/j.cnki.nxdz.000062.

28. S. Wang, Y. Ke, F. Jin, Y. Li, and Z. Jin, "Reasonable Designed Graphdiyne/$AgCoO_2$ S-Scheme Heterojunction for Efficient Photocatalytic Hydrogen Production," *Materials Today Chemistry* 43 (2025): 102450, https://doi.org/10.1016/j.mtchem.2024.102450.

29. X. Wang, Z. Jin, and X. Li, "Monoclinic β-$AgVO_3$ Coupled With CdS Formed a 1D/1D p-n Heterojunction for Efficient Photocatalytic Hydrogen Evolution," *Rare Metals* 42, no. 5 (2023): 1494–1507, https://doi.org/10.1007/s12598-022-02183-y.

30. Z. Chen, L. Wang, X. Jiao, Y. Xia, and D. Chen, "Defect-Mediated Spatial Confinement of Pt Single Atoms on Photoactive $CdIn_2S_4$ Octahedrons: Synergistic Carrier Dynamics Optimization for Photocatalytic Hydrogen Production," *Chemical Engineering Journal* 517 (2025): 164289, https://doi.org/10.1016/j.cej.2025.164289.

31. X. Zhao, J. Wang, J. Kang, X. Wang, H. Yu, and C. Du, "Ni Nanoparticles Anchoring on Vacuum Treated Mo_2TiC_2T MXene for Enhanced Hydrogen Evolution Activity," *Chinese Journal of Structural Chemistry* 42, no. 10 (2023): 100159, https://doi.org/10.1016/j.cjsc.2023.100159.

32. S. Liu, Y. Xiang, J. Liu, et al., "Hydrogen Spillover in Pt/$Ni(OH)_2$/Mo_2TiC_2T Electrocatalyst Improves pH-Universal Hydrogen Evolution Reaction," *International Journal of Hydrogen Energy* 63 (2024): 500–509, https://doi.org/10.1016/j.ijhydene.2024.03.209.

33. C. Yang, X. Li, M. li, and Z. Jin, "Anchoring Oxidation Co-Catalyst Over $CuMn_2O_4$/Graphdiyne S-Scheme Heterojunction to Promote Eosin-Sensitized Photocatalytic Hydrogen Evolution," *Chinese Journal of Catalysis* 56 (2024): 88–103, https://doi.org/10.1016/s1872-2067(23)64563-2.

34. H. Zhang, C. Li, L. Wang, et al., "Efficient Continuous Synthesis of 2-Hydroxycarbazole and 4-Hydroxycarbazole in a Millimeter Scale Photoreactor," *Chinese Chemical Letters* 35, no. 9 (2024): 109351, https://doi.org/10.1016/j.cclet.2023.109351.

35. C. Li, G. Ding, X. Liu, et al., "Photocatalysis Over NH_2-UiO-66/$CoFe_2O_4/CdIn_2S_4$ Double p-n Junction: Significantly Promoting Photocatalytic Performance by Double Internal Electric Fields," *Chemical Engineering Journal* 435 (2022): 134740, https://doi.org/10.1016/j.cej.2022.134740.

36. M. Hamza, J. Evans, G. Andersson, G. Metha, and C. Shearer, "Ultrathin Ru-$CdIn_2S_4$ Nanosheets for Simultaneous Photocatalytic Green Hydrogen Production and Selective Oxidation of Furfuryl Alcohol to Furfural," *Chemical Engineering Journal* 493 (2024): 152603, https://doi.org/10.1016/j.cej.2024.152603.

37. Z. Liu, S. Fan, X. Li, et al., "Synergistic Effect of Single-Atom Cu and Hierarchical Polyhedron-Like $Ta_3N_5/CdIn_2S_4$ S-Scheme Heterojunction for Boosting Photocatalytic NH_3 Synthesis," *Applied Catalysis B: Environment and Energy* 327 (2023): 122416, https://doi.org/10.1016/j.apcatb.2023.122416.

38. U. Fatima, M. Tahir, M. Sagir, and M. Arif, "The Synthesis of Nickel Ferrite $NiFe_2O_4/Ti_3C_2$ MXene Composite for the Photocatalytic Evolution of Hydrogen," *International Journal of Hydrogen Energy* 74 (2024): 316–321, https://doi.org/10.1016/j.ijhydene.2024.06.179.

39. K. Umer, B. Li, H. Shahid, et al., "Electrostatically Engineered $Ni_4POM/Mn_{0.2}Cd_{0.8}S$ Through 1,4-Benzene Dicarboxylic Acid for Efficient Photocatalytic Hydrogen Production," *Applied Catalysis B: Environment and Energy* 373 (2025): 125357, https://doi.org/10.1016/j.apcatb.2025.125357.

40. X. Zhao, X. Bai, R. Zhai, et al., "Trap Engineering in Violet Antimony Phosphorus: Modulating Photoelectron Transfer Pathways for Enhanced Photocatalytic Hydrogen Evolution," *Applied Catalysis B: Environment and Energy* 370 (2025): 125166, https://doi.org/10.1016/j.apcatb.2025.125166.

41. Z. Jin, H. Li, and J. Li, "Efficient Photocatalytic Hydrogen Evolution Over Graphdiyne Boosted With a Cobalt Sulfide Formed S-Scheme Heterojunctions," *Chinese Journal of Catalysis* 43, no. 2 (2022): 303–315, https://doi.org/10.1016/s1872-2067(21)63818-4.

42. X. Huang, Z. He, Y. Chen, et al., "Solid Superacid Catalysts Promote high-Performance Carbon Dots With Narrow-Band Fluorescence Emission for Luminescence Solar Concentrators," *Chinese Chemical Letters* 35, no. 6 (2024): 109271, https://doi.org/10.1016/j.cclet.2023.109271.

43. G. Ren, J. Zhao, Z. Zhao, et al., "Defects-Induced Single-Atom Anchoring on Metal-Organic Frameworks for High-Efficiency Photocatalytic Nitrogen Reduction," *Angewandte Chemie International Edition* 63, no. 2 (2024): e202314408, https://doi.org/10.1002/anie.202314408.

44. Z. Chen, J. Deng, Y. Zheng, W. Zhang, L. Dong, and Z. Chen, "Modulation of Ketyl Radical Reactivity to Mediate the Selective Synthesis of Coupling and Carbonyl Compounds," *Chinese Journal of Catalysis* 61 (2024): 135–143, https://doi.org/10.1016/s1872-2067(24)60045-8.

45. Z. Ma, X. Kuang, S. Peng, and Y. Li, "Manipulating Precursor to Anchor Mo_3S_9 Cluster Onto Carbon Nitride for Photocatalytic H_2 Production," *Advanced Functional Materials* 35, no. 38 (2025): 2425117, https://doi.org/10.1002/adfm.202425117.

46. Z. Zhou, J. Wang, M. Reheimujiang, and Z. Jin, "Graphdiyne/Hierarchical Flower-Like $Sr_2Co_2O_5$ S-Scheme Heterojunction for Enhanced Photocatalytic Hydrogen Evolution," *Journal of Materials Science & Technology* 213 (2025): 241–251, https://doi.org/10.1016/j.jmst.2024.05.080.

47. K. Tu, H. Lin, J. Chou, and J. Wu, "Unveiling the Flexocatalytic Potential of Wide-Bandgap Spinel Oxides: Light-Free Hydrogen Evolution via Strain-Induced Polarization and Oxygen Vacancy Engineering," *Advanced Functional Materials* 35, no. 31 (2025): 2424279, https://doi.org/10.1002/adfm.202424279.

48. L. An, Z. Zhang, G. Liu, et al., "Recent Advances in Transition Metal Electrocatalysts for Effective Nitrogen Reduction Reaction Under Ambient Conditions," *EcoEnergy* 2 (2024): 229–257, https://doi.org/10.1002/ece2.39.

49. S. Xu, M. Li, Y. Wang, C. Gao, R. Xu, and Z. Jin, "Efficient Hydrogen Production over Nitrogen and Sulfur Co-Doped Coal-Based Carbon Quantum Dots Photocatalyst," *Journal of Rare Earths* 42, no. 5 (2024): 838–850, https://doi.org/10.1016/j.jre.2023.09.020.

50. C. Zhuang, C. Yuan, W. Li, et al., "Light-Induced Variation of Lithium Coordination Environment in g-C_3N_4 Nanosheet for Highly Efficient Oxygen Reduction Reactions," *ACS Nano* 18, no. 6 (2024): 5206–5217, https://doi.org/10.1021/acsnano.4c00217.

51. M. Li, J. Wang, and Z. Jin, "Graphdiyne (C_nH_{2n-2}) as an "Electron Transfer Bridge" Boosting Photocatalytic Hydrogen Evolution Over $Zn_{0.5}Co_{0.5}S/MoS_2$ S-Scheme Heterojunction," *Rare Metals* 43, no. 5 (2024): 1999–2014, https://doi.org/10.1007/s12598-023-02539-y.

52. L. Yang, W. Zhou, M. Dou, et al., "Conjugated Polyelectrolytes/Sucrose-Doped Hydroxyl-Rich Carbon Nitride Heterojunctions for Photocatalytic Hydrogen Evolution: Morphology Control, Interfacial Modulation, and Energy Band Engineering," *Advanced Functional Materials* 35, no. 41 (2025): 2500415, https://doi.org/10.1002/adfm.202500415.

53. Y. Cao, L. Ye, Y. Yuan, et al., "Ni-N Bonds Boost S-Scheme Charge Transfer in NiSe/Cv-C_3N_5 for Efficient Water Splitting," *Chinese Journal of Catalysis* 78 (2025): 229–241, https://doi.org/10.1016/s1872-2067(25)64832-7.

54. M. Zhang, Y. Zhang, L. Ye, et al., "In Situ Fabrication $Ti_3C_2F_x$ MXene/$CdIn_2S_4$ Schottky Junction for Photocatalytic Oxidation of HMF to DFF Under Visible Light," *Applied Catalysis B: Environment and Energy* 330 (2023): 122635, https://doi.org/10.1016/j.apcatb.2023.122635.

55. A. Khan, M. Le Pivert, A. Ranjbari, et al., "Cu-Based MOF/TiO_2 Composite Nanomaterials for Photocatalytic Hydrogen Generation and the Role of Copper," *Advanced Functional Materials* (2025): 2501736, https://doi.org/10.1002/adfm.202501736.

56. X. Wang, S. Xue, T. Shi, et al., "Localized Phosphorization Manipulating Internal Electric Field Orientation in Carbon Nitride Homojunction for Efficient Photocatalytic Hydrogen Evolution," *Advanced Functional Materials* 35 (2025): 2424853, https://doi.org/10.1002/adfm.202424853.

57. Y. Zhu, H. Chen, L. Wang, et al., "Construction of ZnO@CDs@Co_3O_4 Sandwich Heterostructure With Multi-Interfacial Electron-Transfer Toward Enhanced Photocatalytic CO_2 Reduction," *Chinese Chemical Letters* 35, no. 4 (2024): 108884, https://doi.org/10.1016/j.cclet.2023.108884.

58. Z. Jin, Z. Liu, and Y. Zhang, "Preparation Method of Graphdiyne and Application of Photocatalytic Hydrogen Production," *Journal of Xihua University (Natural Science Edition)* 44 (2025): 1–17, https://doi.org/10.12198/j.issn.1673−159X.5718.

59. G. Nuroldayeva, T. Umurzak, A. Kireyeva, et al., "A Comparative Study of Bulk and Surface W-Doped High-Ni Cathode Materials for Lithium-Ion Batteries," *Nanoscale* 17, no. 13 (2025): 8192–8205, https://doi.org/10.1039/d4nr04691a.

60. X. Wang, Y. Li, T. Li, and Z. Jin, "Synergistic Effect of Bimetallic Sulfide Enhances the Performance of CdS Photocatalytic Hydrogen Evolution," *Advanced Sustainable System* 7, no. 1 (2023): 2200139, https://doi.org/10.1002/adsu.202200139.

61. J. Wang, S. He, M. Zhang, et al., "In-Situ Constructing Eosin Y Sensitized $Cs_2PtSnCl_6$ Perovskites for Enhanced Photocatalytic Hydrogen Evolution," *Advanced Energy Materials* 15, no. 25 (2025): 2406048, https://doi.org/10.1002/aenm.202406048.

62. J. Sun, Y. Zheng, Z. Zhang, X. Meng, and Z. Li, "Modulation of d-Orbital to Realize Enriched Electronic Cobalt Sites in Cobalt Sulfide for Enhanced Hydrogen Evolution in Electrocatalytic Water/Seawater Splitting," *Rare Metals* 43, no. 2 (2023): 511–521, https://doi.org/10.1007/s12598-023-02427-5.

63. K. Wang, S. Liu, Y. Li, G. Wang, M. Yang, and Z. Jin, "Phosphorus ZIF-67@NiAl LDH S-Scheme Heterojunction for Efficient Photocatalytic Hydrogen Production," *Applied Surface Science* 601 (2022): 154174, https://doi.org/10.1016/j.apsusc.2022.154174.

64. W. Zhang, Z. Jin, and Z. Chen, "Rational-Designed Principles for Electrochemical and Photoelectrochemical Upgrading of CO_2 to Value-Added Chemicals," *Advanced Science* 9 (2022): 2105204, https://doi.org/10.1002/advs.202105204.

65. J. Ran, L. Chen, D. Wang, et al., "Atomic-Level Regulated 2D $ReSe_2$: A Universal Platform Boostin Photocatalysis," *Advanced Materials* 35, no. 19 (2023): 2210164, https://doi.org/10.1002/adma.202210164.

66. H. Zhao, M. Wang, H. Zhu, and J. Dou, "Construction of LDH-Derived CoNiP Modified W/Z-CdS Homojunction for Improved Photocatalytic Hydrogen Evolution: Achieving Broad Solar Light Response and Multiple Phases Charge Transfer," *Separation and Purification Technology* 357 (2025): 130224, https://doi.org/10.1016/j.seppur.2024.130224.

67. D. Zou, W. Zhao, Y. Xu, X. Li, Y. Liu, and C. Yang, "Dual Transmission Channels at Metal-MoS_2/WSe_2 Hetero-Bilayer Interfaces," *Physical Chemistry Chemical Physics* 25 (2023): 16896–16907, https://doi.org/10.1039/d3cp00710c.

68. Y. Liu, X. Chu, Y. Jiang, et al., "Self-Accelerating H_2 Evolution Activity by in Situ Transformation on Noble-Metal-Free Photocatalyst of Covalent Organic Framework and Cu_2O Composite," *Advanced Functional Materials* 34, no. 25 (2024): 2316546, https://doi.org/10.1002/adfm.202316546.

69. X. Lv, P. Hong, J. Wen, Y. Ma, C. Spataru, and Y. Weng, "Highly Efficient Operation of an Innovative SOFC Powered All-Electric Ship System Using Quick Approach for Ammonia to Hydrogen," *Frontiers in Energy* 19, no. 3 (2025): 365–381, https://doi.org/10.1007/s11708-025-0974-8.

70. C. Zheng, G. Jiang, Y. Li, and Z. Jin, "NiO and $Co_{1.29}Ni_{1.71}O_4$ Derived From NiCo LDH Form S-Scheme Heterojunction for Efficient Photocatalytic Hydrogen Evolution," *Journal of Alloys and Compounds* 904 (2022): 164041, https://doi.org/10.1016/j.jallcom.2022.164041.

71. C. Wang, F. Zheng, L. Zhang, J. Yang, and P. Dong, "Insight Into the Role of Graphene Quantum Dots on the Boosted Photocatalytic H_2 Production Performance of a Covalent Organic Framework," *Applied Surface Science* 640 (2023): 158383, https://doi.org/10.1016/j.apsusc.2023.158383.

72. Y. Ke, S. Wang, F. Jin, G. Liu, Z. Jin, and N. Tsubaki, "Charge Transfer Optimization: Role of Cu-Graphdiyne/$NiCoMoO_4$ S-Scheme Heterojunction and Ohmic Junction," *Chinese Journal of Structural Chemistry* 43, no. 12 (2024): 100458, https://doi.org/10.1016/j.cjsc.2024.100458.

73. Q. Chen, J. Huang, D. Chu, et al., "Accelerated Photogenerated Charge Separation Driven Synergistically by the Interfacial Electric Field and Work Function in Z-Scheme Zn-Ni_2P/G-C_3N_4 for Efficient Photocatalytic Hydrogen Evolution," *Exploration* 5 (2025): 20240189, https://doi.org/10.1002/exp.20240189.

74. M. Zhu, S. Kim, L. Mao, et al., "Metal-Free Photocatalyst for H_2 Evolution in Visible to Near-Infrared Region: Black Phosphorus/Graphitic Carbon Nitride," *Journal of the American Chemical Society* 139, no. 37 (2017): 13234–13242, https://doi.org/10.1021/jacs.7b08416.

75. Y. Zhou, P. Dong, J. Liu, et al., "Functional Groups-Dependent Tp-Based COF/$MgIn_2S_4$ S-Scheme Heterojunction for Photocatalytic

Hydrogen Evolution," *Advanced Functional Materials* 35, no. 30 (2025): 2500733, https://doi.org/10.1002/adfm.202500733.

76. X. Zhao, Y. Cao, M. Lei, Z. Jin, and N. Tsubaki, "Constructing S-Scheme Heterojunctions by Integrating Covalent Organic Frameworks With Transition Metal Sulfides for Efficient Noble-Metal-Free Photocatalytic Hydrogen Evolution," *Acta Physico-Chimica Sinica* 41, no. 12 (2025): 100152, https://doi.org/10.1016/j.actphy.2025.100152.

77. H. Yin, J. Du, X. Ma, Y. Li, and Z. Jin, "Efficient Photocatalytic Hydrogen Production Through Mn0.4Cd0.6S/2D Mo2TiC2 MXene Ohm Junction With Effective Light Corrosion Resistance," *Advanced Sustainable System* (2025): 202501465.

78. X. Zhao, L. Zhang, G. Liu, Z. Jin, G. Yang, and N. Tsubaki, "Graphdiyne Based Heterojunction for Photocatalytic Hydrogen Production," *Inorganic Chemistry Frontiers* (2025), https://doi.org/10.1039/d5qi01835h.

79. B. Yang, F. Jin, and Z. Jin, "Efficient Photocatalytic Hydrogen Production by Heterojunction Strategy With Covalent Organic Frameworks Loaded With Non-Precious Metal Semiconductors," *Chinese Journal of Catalysis* 81 (2026): 172–184, https://doi.org/10.1016/s1872-2067(25)64904-7.

80. J. Gao, X. Lin, B. Jiang, et al., "Epitaxial Vertical Growth of Carbon Nitride-Based Homojunction Composites for Enhanced Photocatalytic Degradation of Tetracycline Hydrochloride," *Chemical Research in Chinese Universities* 41, no. 4 (2025): 868–879, https://doi.org/10.1007/s40242-025-5111-z.